Seismic velocity and anisotropy of the uppermost mantle beneath Madagascar from Pn tomography

Fenitra Andriampenomanana, Andrew Nyblade, Michael Wysession, Raymond Durrheim, Frederik Tilmann, Guilhem Barruol, Gérard Rambolamanana, Tsiriandrimanana Rakotondraibe

Geophysical Journal International

Geophys. J. Int. (2020) **224,** 290–305
Advance Access publication 2020 September 24
GJI Seismology

doi: 10.1093/gji/ggaa458

Seismic velocity and anisotropy of the uppermost mantle beneath Madagascar from *Pn* tomography

Fenitra Andriampenomanana [1,2] Andrew A. Nyblade,[1,3] Michael E. Wysession,[4] Raymond J. Durrheim,[1] Frederik Tilmann [5,6] Guilhem Barruol [7] Gérard Rambolamanana[8] and Tsiriandrimanana Rakotondraibe[1,2]

[1] *School of Geosciences, University of the Witwatersrand, Private Bag* 3 - *Wits* 2050, *Johannesburg, South Africa. E-mail: nyonyfenitra@gmail.com*
[2] *Institut et Observatoire de Géophysique d'Antananarivo, Université d'Antananarivo, Ambohidempona - B.P* 3843, *Antananarivo* 101, *Madagascar*
[3] *Department of Geosciences, Penn State University, University Park, PA* 16802, *USA*
[4] *Department of Earth and Planetary Sciences, Washington University in St. Louis, Campus Box* 1169, 1 *Brookings Dr, Saint Louis, MO* 63130–4899, *USA*
[5] *Helmholtzzentrum Potsdam. Deutsches GeoForschungs Zentrum (GFZ), Telegrafenberg,* 14473 *Potsdam, Germany*
[6] *Freie Universität Berlin, Berlin, Germany*
[7] *Université de Paris, Institut de physique du globe de Paris, CNRS, UMR* 7154, *F-*75005 *Paris, France*
[8] *Preparatory Commission for the Comprehensive Nuclear-Test-Ban Treaty Organization (CTBTO)* , 1400 *Vienna, Austria*

Accepted 2020 September 22. Received 2020 August 7; in original form 2019 November 5

SUMMARY

The lithosphere of Madagascar records a long series of tectonic processes. Structures initially inherited from the Pan-African Orogeny are overprinted by a series of extensional tectonic and magmatic events that began with the breakup of Gondwana and continued through to the present. Here, we present a *Pn*-tomography study in which *Pn* traveltimes are inverted to investigate the lateral variation of the seismic velocity and anisotropy within the uppermost mantle beneath Madagascar. Results show that the *Pn* velocities within the uppermost mantle vary by ± 0.30 km s^{-1} about a mean of 8.10 km s^{-1}. Low-*Pn*-velocity zones (<8.00 km s^{-1}) are observed beneath the Cenozoic alkaline volcanic provinces in the northern and central regions. They correspond to thermally perturbed zones, where temperatures are estimated to be elevated by ∼100–300 K. Moderately low *Pn* velocities are found near the southern volcanic province and along an E–W belt in central Madagascar. This belt is located at the edge of a broader low *S*-velocity anomaly in the mantle imaged in a recent surface wave tomographic study. High-*Pn*-velocity zones (>8.20 km s^{-1}) coincide with stable and less seismically active regions. The pattern of *Pn* anisotropy is very complex, with small-scale variations in both the amplitude and the fast-axis direction, and generally reflects the complicated tectonic history of Madagascar. *Pn* anisotropy and shear wave (*SKS*) splitting measurements show good correlations in the southern parts of Madagascar, indicating coherency in the vertical distribution of lithospheric deformation along Pan-African shear zone as well as coupling between the crust and mantle when the shear zones were active. In most other regions, discrepancies between *Pn* anisotropy and *SKS* measurements suggest that the seismic anisotropy in the uppermost mantle beneath Madagascar differs from the vertically integrated upper mantle anisotropy, implying a present-day vertical partitioning of the deformation. *Pn* anisotropy directions lack the coherent pattern expected for an incipient plate boundary within Madagascar proposed in some kinematic models of the region.

Key words: Seismic anisotropy; Seismic tomography; Dynamics of lithosphere and mantle.

1 INTRODUCTION

The Precambrian lithosphere of Madagascar was shaped mainly by the Neoproterozoic to Cambrian Pan-African Orogeny during the amalgamation of Gondwana (e.g. Collins 2006). During the Mesozoic, there were rifting events that led to the separation of Madagascar from Africa and India (e.g. Rabinowitz *et al.* 1983), and in the Cenozoic, volcanism has occurred in at least three regions (e.g. Emerick & Duncan 1982). A number of recent studies have investigated the seismic structure of the crust and upper mantle (e.g. Rindraharisaona *et al*. 2013, 2017; Andriampenomanana *et al.* 2017; Pratt *et al.* 2017), the seismicity and seismotectonics of the

island (e.g. Rindraharisaona *et al.* 2013; Rakotondraibe *et al.* 2020) and its plate kinematics (e.g. Saria *et al.* 2013; Stamps *et al.* 2014, 2015, 2018), greatly improving our understanding of the structure and geodynamics of Madagascar.

One of the major findings from seismic imaging of the upper mantle beneath Madagascar is the presence of several low-velocity regions that correlate spatially with Cenozoic magmatism, indicating that the cause of the magmatism is linked to sublithospheric mantle processes (Pratt *et al.* 2017). Upper mantle strain mapped from shear wave splitting measurements reveals a complex pattern of seismic anisotropy in Madagascar (e.g. Reiss *et al.* 2016; Ramirez *et al.* 2018; Scholz *et al.* 2018), which has been interpreted in terms of both active sublithospheric mantle flow and fossil anisotropy within the lithosphere. These studies, however, leave unresolved a number of questions about the nature of the lithospheric mantle, which are the focus of this study: (1) to what extent has the uppermost mantle been thermally modified by geodynamic processes giving rise to the Cenozoic magmatism, (2) how is strain distributed within the lithosphere and (3) to what extent does anisotropy, pervasively frozen within the lithosphere, contribute to the pattern of seismic anisotropy obtained from shear wave splitting measurements?

To address these questions, we tomographically image the uppermost mantle beneath Madagascar using *Pn* traveltimes. *Pn* seismic phases represent waves generated at regional distances that are refracted in the uppermost mantle. Most of the *Pn* energy travels horizontally in the few kilometres immediately beneath the Moho discontinuity (e.g. Hearn & Ni 1994). By combining refracted *Pn* waves travelling along various azimuths, the azimuthal anisotropy in *Pn*-wave velocity propagation can be determined (e.g. Bamford 1977). The patterns in *Pn* velocity and anisotropy that we obtain provide new insights into the seismic properties of the uppermost mantle and its pervasive deformation beneath much of Madagascar and help to constrain the location and magnitude of thermal anomalies as well as the anisotropic fabric of the lithospheric mantle.

2 TECTONIC BACKGROUND

The lithosphere of Madagascar, which initially formed during the amalgamation of Gondwana in the Late Neoproterozoic and Early Cambrian (*ca.* 570–510 Ma) (e.g. Shackleton 1996), can be divided into two regions: Precambrian basement that crops out over the eastern two-thirds of the island and Carboniferous-to-present day sedimentary basins in the western third of the island. The Precambrian basement is divided into six Palaeoarchean to Neoproterozoic domains/provinces: the Bemarivo, Antananarivo, Ikalamavony, Anosyen-Androyen and Vohibory domains, and the Antongil-Masora craton (Fig. 1, e.g. Collins 2006; Tucker *et al.* 2011). These provinces are cut by several N–S or NW–SE trending crustal-scale shear zones (Fig. 1). Most shear zones represent the boundaries of major geological domains (e.g. the Sandrakota, Ranotsara, Beraketa, and Ampanihy shear zones), although others lie within domains (e.g. the Angavo-Ifanadiana, Zazafotsy, and Ihosy shear zones) (e.g. Martelat *et al.* 2000, 2014). The western third of the island consists of three Carboniferous-to-present-day sedimentary basins: the Antsiranana, Mahajanga, and Morondava basins, which are underlain by Precambrian basement (e.g. Besairie 1971). The rift system associated with the breakup of Gondwana during the Late Jurassic and Early Cretaceous (*ca.* 150 Ma, e.g. Rabinowitz *et al.* 1983) stretched and thinned the crust (e.g. Andriampenomanana *et al.* 2017) while forming sedimentary basins.

Although Madagascar has not experienced any major tectonic activity for the past 85 Myr and has been far from active plate boundaries, recent Cenozoic volcanic provinces (as young as <1 Ma), are found in three regions: (1) in Nosy Be Island, Massif d'Ambre, and Massif du Tsaratanàna in the northern region (e.g. Emerick & Duncan 1982; Bushwaldt *et al.* 2005); (2) around Itasy and Ankaratra in the central region (e.g. Nougier *et al.* 1986; Melluso *et al.* 2018) and (3) around Ankililoaka in the southwestern region of Madagascar (Bardintzeff *et al.* 2010, Fig. 1). These three young volcanic provinces consist mainly of alkali basalts that erupted between *ca.* 28 and 1 Ma (e.g. Emerick & Duncan 1982; Nougier *et al.* 1986), and are known as the Northern Madagascar Alkaline Province (NMAP), the Central Madagascar Alkaline Province (CMAP) and the Southern Madagascar Alkaline Province (SMAP), respectively (e.g. Pratt *et al.* 2017, Fig. 1). The origin of the Cenozoic magmatic activity has long been and is still debated. Some researchers have related the volcanism to lithospheric processes, for example, Nougier *et al.* (1986), who associated the volcanism with fracture zones that formed during the Mesozoic rifting of Madagascar. Others have linked the volcanism to the Comores magmatic province (Emerick & Duncan 1982) or the southern extent of the East African Rift (e.g. Saria *et al.* 2013; Stamps *et al.* 2015; Michon 2016). Notably, a seismo-volcanic crisis started in June 2018 and is still ongoing in the very neighbourhood of the island of Mayotte, *ca.* 400 km west of northern Madagascar (Cesca *et al.* 2020).

The crust and the upper mantle of Madagascar were recently studied by Pratt *et al.* (2017), who conducted a surface wave tomography study. Their model revealed upper mantle low-shear-velocity zones that extend from the base of the crust to a depth of at least 150 km beneath NMAP and CMAP and depths between 50 and 150 km beneath SMAP. These low-velocity zones were attributed to asthenospheric upwelling induced by delamination of the mantle lithosphere, which caused the Cenozoic magmatic activity and led to regional uplift. Similar results have been reported by studies that jointly inverted receiver functions and surface wave dispersion measurements (Rindraharisaona *et al.* 2013; Andriampenomanana *et al.* 2017), revealing slow upper mantle velocities beneath the NMAP, CMAP and SMAP.

A number of recent studies have also investigated Madagascar's upper mantle seismic anisotropy. Shear wave splitting measurements and waveform modeling of *SKS* phases by Reiss *et al.* (2016) revealed NE-oriented fast *S*-polarization directions in the southcentral region of Madagascar, which they attributed to asthenospheric flow aligned with surface plate motion and a NW fast-polarization direction, which they attributed to crustal anisotropy within a ∼150-km-wide ductile shear zone. Ramirez *et al.* (2018), also using teleseismic shear wave splitting measurements, reported a very complex pattern of fast polarization directions across the island that they attributed to a combination of mantle flow (from the African superplume, the Comores hotspot and lithosphere delamination) and fossil anisotropy from ancient collisional and shear events. This complex pattern of anisotropy is also confirmed by *SKS* splitting measurements calculated for stations deployed within southeastern Madagascar (Scholz *et al.* 2018). By analyzing crustal radial anisotropy in southcentral Madagascar, Dreiling *et al.* (2018) found evidence of crustal anisotropy at different vertical levels of the crust. They attributed the anisotropy in the upper crust to shallowly dipping layers, possibly associated with an imbricated nappe stack, and the anisotropy in the middle crust to strongly folded and vertical shear zones; in the lower crust the radial anisotropy was related to

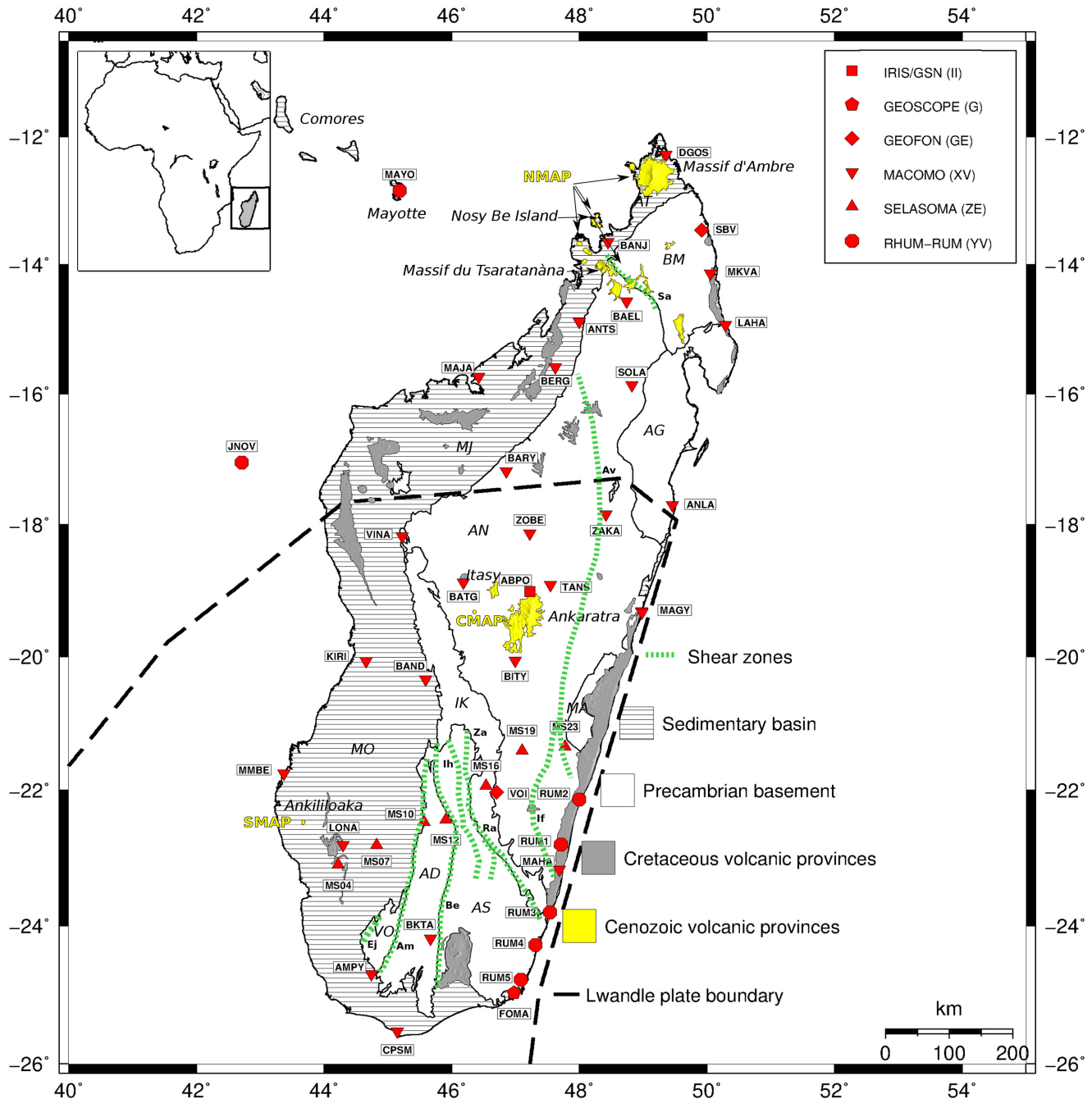

Figure 1. A simplified geologic map of Madagascar showing the different geological units, volcanic provinces, shear zones, seismic networks and place-names referred to in the text [modified from Tucker *et al.* (2012)]. Red symbols show permanent and temporary broad-band seismic stations used in this study. Also plotted is the Lwandle Plate boundary (black dashed line) after Saria *et al.* (2014). Geological features include Precambrian basement: *AD*—Androyen domain, *AG*—Antongil craton, *AN*—Antananarivo domain, *AS*—Anosyen domain, *BM*—Bemarivo domain, *IK*—Ikalamavony domain, *MA*—Masora craton, and *VO*—Vohibory domain; Sedimentary basins: *AT*—Antsiranana basin, *MJ*—Mahajanga basin, and *MO*—Morondava basin. The most prominent shear zones are shown on the map: Am—Ampanihy, Av—Angavo, Be—Beraketa, Ej—Ejeda, If—Ifanadiana, Ih—Ihosy, Ra—Ranotsara, Sa—Sandrakota and Za—Zazafotsy. NMAP/CMAP/SMAP: Northern/Central/Southern Madagascar Alkaline Province.

the orogenic collapse following the formation of the Pan-African Orogen. Rajaonarison *et al.* (2020), using the numerical modeling of mantle flow, suggested that the observed seismic anisotropy in the northern and southern regions of Madagascar (Reiss *et al.* 2016; Ramirez *et al.* 2018; Scholz *et al.* 2018) can be explained, at least in part, by edge-driven convection within the asthenosphere. They also proposed that fossil anisotropy associated with shear zones may contribute to the seismic anisotropy in the southern region, whereas in central Madagascar the anisotropic patterns are controlled by the interaction of the edge-driven convection with the localized low-velocity-zone (Pratt *et al.* 2017). All these independent studies document the complex structure of the Malagasy lithosphere and the complex lateral and vertical distribution of seismic anisotropy.

3 DATA

No seismic catalogue covering all of Madagascar was available until the early 2010s, when temporary seismic networks were deployed. As a result, data used in this study consist of *Pn* first-arrival times hand-picked from local and regional earthquakes that occurred in and around Madagascar recorded by the MAdagascar-COmores-MOzambique (MACOMO) project (https://doi.org/10.7914/SN/XV_2011; Wysession *et al.* 2011), which deployed 26 broad-band seismic stations in Madagascar between 2011 and 2013: 10 of the stations recorded seismic data for two years starting in September 2011, while the remaining 16 recorded for one year, starting in September 2012 (Fig. 1). *Pn* arrivals were also picked on four permanent broad-band stations: ABPO (https://doi.org/10.7914/SN/II; Scripps Institution of Oceanography 1986), FOMA (https://doi.org/10.18715/GEOSCOPE.G; Institut de Physique du Globe de Paris (IPGP) & Ecole et Observatoire des Sciences de la Terre de Strasbourg (EOST) 1982), and VOI and SBV (https://doi.org/10.14470/TR560404; GEOFON Data Centre 1993), for the same time interval (September 2011 to September 2013). In addition, *Pn* arrivals were picked on several temporary broad-band stations from two other projects to fill a gap in the southern part of Madagascar: seven stations from the SEismological signatures in the Lithosphere/Asthenosphere system of SOuthern MAdagascar (SELASOMA) experiment (https://doi.org/10.14470/MR7567431421; Tilmann *et al.* 2012; from May 2012 to September 2013), and ten stations from the Réunion Hotspot and Upper Mantle—Réunions Unterer Mantel (RHUM-RUM) project (https://doi.org/10.15778/RESIF.YV2011; Barruol & Sigloch 2013; from September 2011 to September 2013, Fig. 1). In summary, a total of 47 seismic stations, well-distributed across Madagascar, including two stations on the Îles Éparses around Madagascar, were used for this study (Fig. 1). Seismic events were located using the earthquake location program HYPOELLIPSE (Lahr 1999) in which the crustal model from Andriampenomanana *et al.* (2017) was used (Rakotondraibe *et al.* 2020).

The following quality control criteria were applied to the *Pn* picks: (1) seismic events had to be inside the seismic network; (2) only arrivals at epicentral distances of >220 km were used [the *Pg*-*Pn* crossover distance for a 35-km-thick crust, the average crustal thickness of Madagascar from Andriampenomanana *et al.* (2017)]; (3) each seismic station must have recorded at least five seismic events; (4) each seismic event must have been recorded on at least five stations; (5) a correction for station elevation was made using a *P* velocity of 5.50 km s^{-1} for the upper crust and (6) a plot of traveltime versus the epicentral distance was fit with a straight line, and then traveltimes with residuals larger than 6 s relative to the best-fitting line were removed. The traveltime versus distance plot and the traveltime residuals relative to the straightline fit are shown in Fig. 2. This process yielded a mean *Pn* velocity of 8.10 km s^{-1}, which is the inverse of the slope of the traveltime versus offset line.

Application of the above selection criteria produced 4963 reliable *Pn* traveltimes from 343 seismic events recorded by 44 seismic stations (see supplemental materials for list of stations and events, Tables S1 and S2, respectively; and Fig. S1 shows typical seismograms used in this study, showing examples of traveltimes that we picked and rejected). *Pn* ray paths and the ray density per grid cell are shown in Fig. 3. As expected, the ray paths show good coverage over most of the Precambrian basement of Madagascar. The extreme northern, western and southern parts of the island are poorly covered.

4 *Pn* TOMOGRAPHY METHOD

Pn phases are waves that are critically refracted at the crust–mantle boundary. As a refracted ray, *Pn* ray paths have three segments: (1) the downgoing source-to-mantle path through the crust, (2) the mostly horizontal passage through the uppermost mantle and (3) the up-going mantle-to-receiver path back through the crust. We used the technique developed by Hearn (1996) to invert the *Pn* traveltimes for variations in the uppermost mantle velocity and the seismic anisotropy.

In this approach, the uppermost mantle surface is divided into a 2-D set of cells for which the uppermost mantle velocity and anisotropy variations are calculated. The traveltime residuals, t_{ij}, of the ray between station i and earthquake j are described as:

$$t_{ij} = a_i + b_j + \sum d_{ijk}\,(s_k + A_k cos2\phi + B_k sin2\phi)\,, \qquad (1)$$

where a_i is the static delay for station i, b_j is the static delay for event j, ϕ is the backazimuth angle, d_{ijk} is the distance traveled by the ray ij in mantle cell k, s_k is the slowness perturbation (the inverse of velocity) and A_k and B_k are two anisotropic coefficients (Hearn 1996).

A regularized least-squares method is used to solve the set of traveltime equations in eq. (1). These multiple traveltime equations are obtained from all the rays between event-station pairs, where the unknowns are the station and event delays (a_i and b_j), the uppermost mantle slowness (s_k), and the two anisotropic coefficients (A_k and B_k). The anisotropy parameters, the magnitude and direction of the fastest wave propagation, within the cell k are estimated by $\sqrt{A_k^2 + B_k^2}$ and $\frac{1}{2}\arctan\left(\frac{B_k}{A_k}\right)$, respectively. Laplacian damping equations are introduced to regularize the solution of eq. (1). The velocity and the anisotropy were separately regularized in the inversion by two damping constants. The smoothness of the velocity is controlled by damping the slowness s_k while the smoothness of the anisotropy is controlled by damping the two anisotropy coefficients, A_k and B_k. The damping coefficients control the trade-off between errors and resolution: typically, low values provide better resolution but large errors, while high damping gives worse resolution but smaller errors.

5 REGULARIZATION OF THE VELOCITY-ANISOTROPY TRADE-OFF, ERROR ESTIMATION, AND RESOLUTION ANALYSIS

Selecting the most appropriate damping parameter is important in the regularized least-square inversion, as it controls the tradeoff between errors and resolution (Hearn 1996). The damping coefficient of the velocity was set first through trial and error by turning off the anisotropy part in the inversion. The coefficient was chosen according to the resolution of the obtained structure, the error observation, as well as the consistency with the geology to avoid over- or underdamping. The surface of the uppermost mantle was gridded into 1/8-degree square cells (0.125° × 0.125°; i.e. about 14 km × 14 km) for solving the set of traveltime equations, and the inversion was run for 100 iterations. After running inversions for a range of damping coefficients, with the anisotropy component turned off, a value of 500 was selected for the damping coefficient because it yielded an acceptable tradeoff between fitting the data and model roughness (Figs S2 and S3).

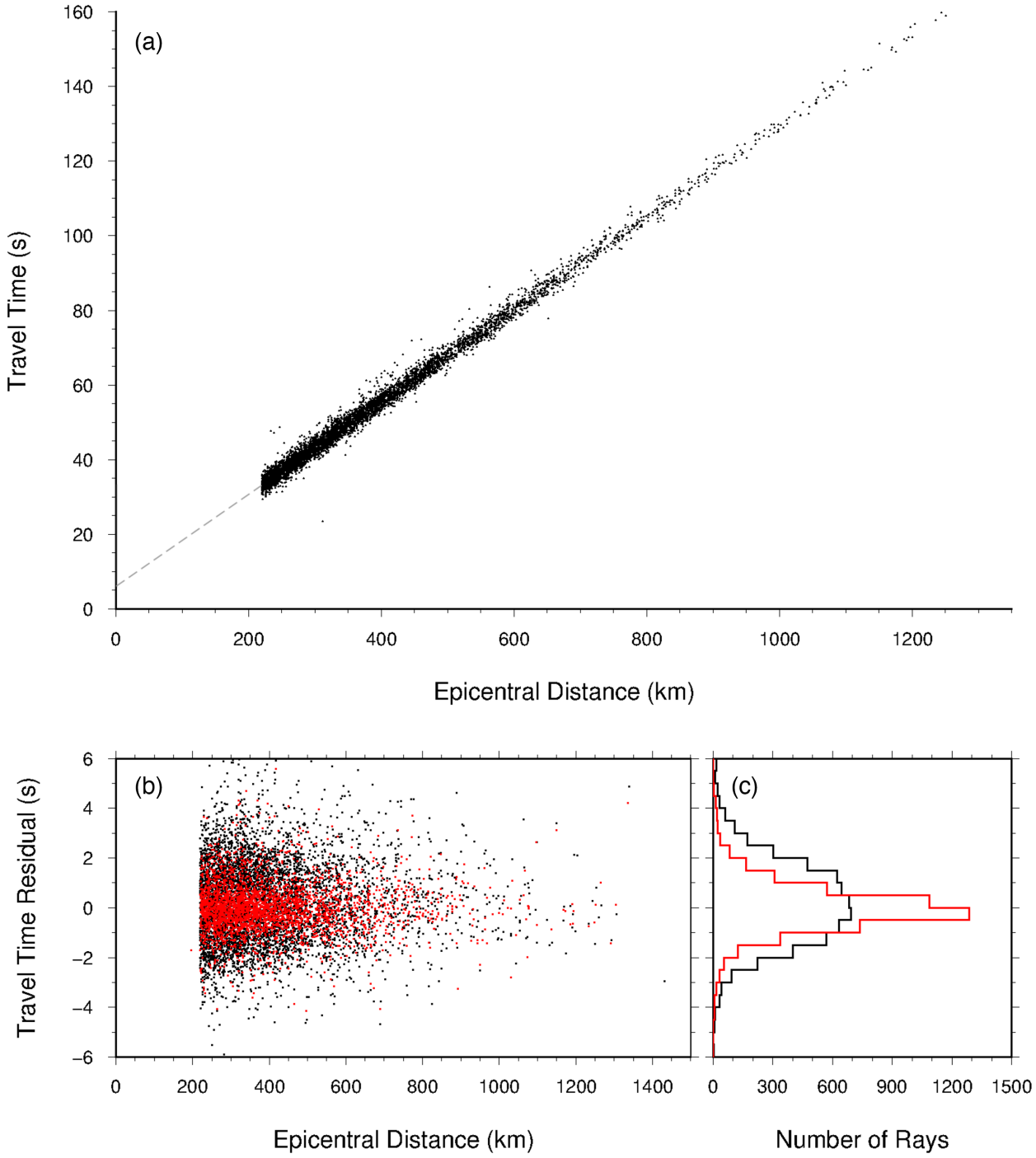

Figure 2. All *Pn* arrivals used for the inversion. (a) Plot of traveltimes versus epicentral distances. A least-squares straight-line fit to the data shows an average *Pn* velocity of 8.1 km s^{-1} (from the inverse of the slope) and an average crustal mean delay of 6.5 s (from the intercept). (b) Plot of the traveltime residuals of each arrival relative to the best-fitting line before (black) and after (red) the inversion. The standard deviation of *Pn* traveltime residuals decreased from 1.71 to 0.99 s after the inversion. (c) Distribution of the traveltime residuals before (black) and after (red) the inversion.

Following the approach of Hearn (1996), the relative trade-off between the velocity variations and the anisotropy variations was examined in order to choose an appropriate damping coefficient for the anisotropy. This involved building two sets of synthetic checkerboard models: the first model was characterized by sinusoidal variations in velocity at a 3° half-wavelength between −0.30 and +0.30 km s^{-1} with no anisotropy variations, and the second model included sinusoidal variations in anisotropy parameters, alternating between N–S and E–W directions with sinusoidal variations in anisotropic strength of 9 per cent at a 3° half-wavelength without velocity variations. Gaussian noise with a standard deviation of 0.7 s was added to the synthetic traveltime. The models were inverted using the traveltimes and ray paths of the actual data with a velocity damping coefficient fixed at 500, as previously

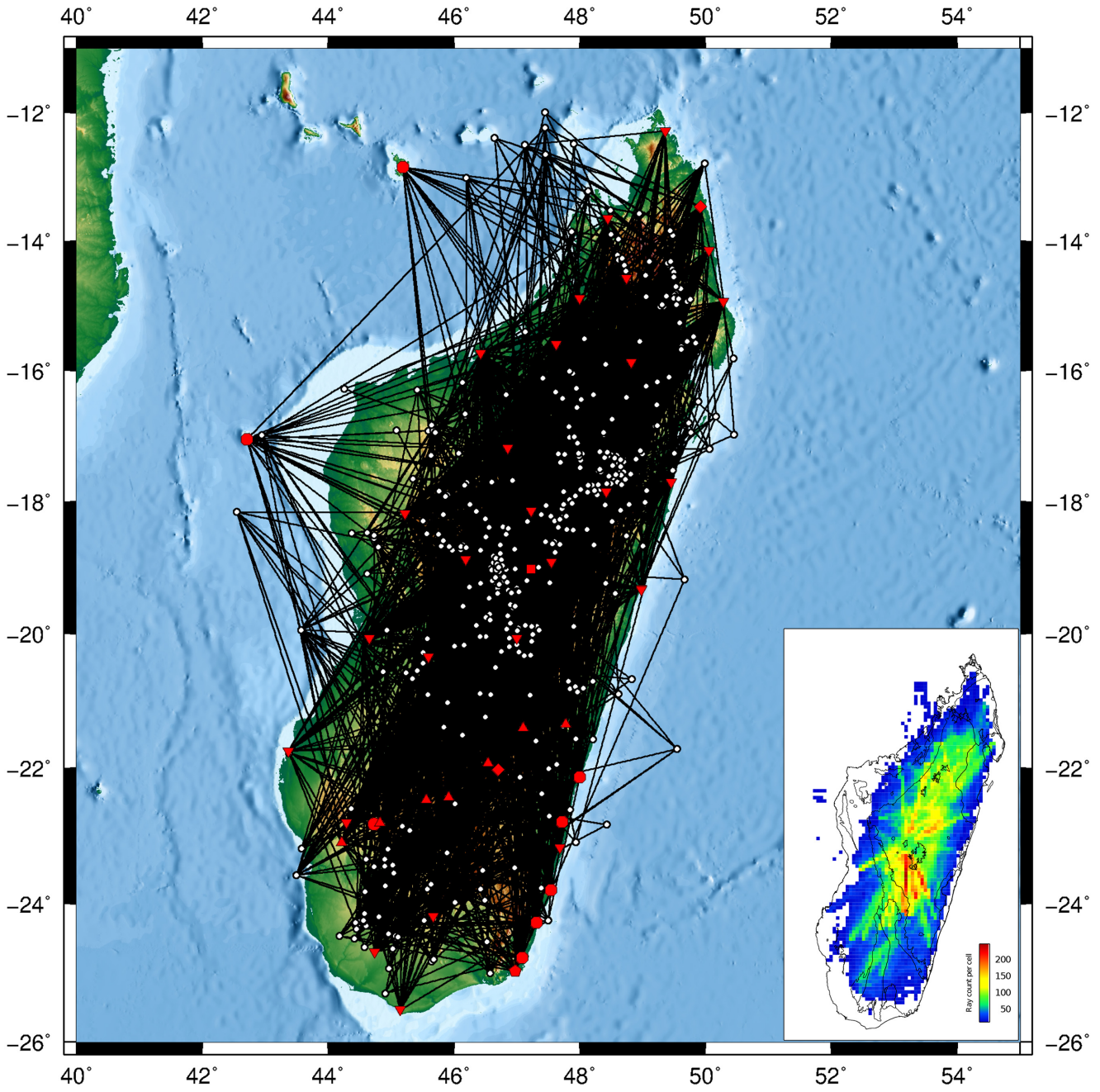

Figure 3. Map showing the seismic stations (red symbols) and seismic events (white dots) selected for the *Pn* tomography study. Black lines show the 4963 *Pn* rays that connect the seismic stations with the seismic events. The eastern Precambrian area is well covered compared to the western sedimentary basins. The map on the bottom corner shows the number of rays per cell (a 1/8-degree square cell or 0.125° × 0.125°; i.e. about 14 km × 14 km); only grid cells that are crossed by at least 10 ray paths are shown here and used in the inversion.

found, with the damping coefficient for the anisotropy calculation changed many times. The inversion was first run for only velocity variations in the test model. The rms values of the velocity (rms_velocity) and anisotropy (rms_anisotropy) magnitude perturbations were calculated for all cells crossed by at least 10 ray paths, as well as the velocity-to-anisotropy trade-off (which is the ratio rms_anisotropy/rms_velocity). The process was then repeated for only anisotropy variations in the test model, and the anisotropy-to-velocity trade-off (which is the ratio rms_velocity/rms_anisotropy) was subsequently obtained. The best value of the anisotropy damping constant is the value that equalizes the velocity-to-anisotropy trade-off and the anisotropy-to-velocity trade-off. From running a number of inversions, it was found that the two curves intersected at a value of around 600 for the anisotropy damping coefficient (Fig. S4). Therefore, damping coefficients of 500 and 600 were chosen for the velocity and anisotropy, respectively, for the final inversions. Fig. S5 shows the fast *Pn*-anisotropy directions obtained from inverting real data using different anisotropy damping coefficients.

The static delays *a* and *b* were inverted undamped in this study, where *a* and *b* depend on the crustal thickness and velocity, as well as errors related to picking, clock, origin time, and depth location.

Undamping the station and event delays helps to reduce or erase the trade-off between these delays and the velocity and anisotropy (Pei *et al.* 2011).

The bootstrap resampling technique (Koch 1992) was used to evaluate the standard error of the inversion. In this technique, *Pn* traveltime data sets are randomly resampled and inverted 100 times (e.g. Hearn & Ni 1994) and the one-standard-deviation error is computed from the resulting bootstrap sample solutions. The rms errors of the traveltime picks after inversion is 0.7 s, which may be partially introduced by heterogeneity within the crust or a strong Moho slope. Additional possible factor contributing to this error could be the 4ϕ term of anisotropy, which is nearly always neglected because of insufficient data coverage and tends to be much smaller than the 2ϕ variation for typical Earth materials. In the well-sampled part of the model, the standard errors are generally around 0.06 km s^{-1} and 1.0 per cent for isotropic velocity and anisotropy, respectively (Fig. 4). The highest errors in velocity ($\sim$0.1 km s^{-1}) correspond to regions where the ray path density is the lowest, especially along the edges of the sampled area.

Other potential sources of error that might impact the velocity model are small-scale heterogeneities within the crust, which would be difficult to quantify; and abrupt changes in Moho depth, which are unlikely because crustal structure studies indicate that lateral changes in Moho topography occur smoothly beneath the island (e.g. Andriampenomanana *et al.* 2017; Rindraharisaona *et al.* 2017).

We used checkerboard tests to assess the influence of ray coverage on the spatial resolution of the model. This involved creating checkers with velocities that vary sinusoidally between -0.30 and $+0.30$ km s^{-1} relative to the average *Pn* velocity (8.10 km s^{-1}). The anisotropy directions were set to alternate between N–S and E–W directions with sinusoidal variations in anisotropy strength of 9 per cent. *Pn* ray paths, seismic stations, and seismic events used for the tomographic inversion of the real data were utilized to compute synthetic *Pn* arrival times. We added Gaussian noise to the synthetic traveltimes with a standard deviation of 0.7 s, which is equivalent to the rms error of the residuals obtained from the actual inversion. The synthetic traveltimes were inverted using parameters identical to those used to invert the real data for a range of square checker sizes (1.00°, 1.25°, 1.50°, 1.75°, 2.00°, 2.25°, 2.50°, 2.75° and 3.00°, Figs S6 and S7). The tests indicate that *Pn* velocities with 1.25° × 1.25° cell sizes can be resolved for most of the study region (Fig. 5a), but the resolution can reach as small as 1.00° × 1.00° in the central part of the island, mostly around the Antananarivo domain, where the density of ray paths is highest. In comparison, the resolution weakens around the edge of the sampled area. The *Pn* anisotropy can be resolved for 2.50° × 2.50° cell sizes for most of the study region, and 1.75° × 1.75° in well-covered areas (Fig. 5b).

6 RESULTS AND DISCUSSION

The results of the *Pn* inversion are shown in Fig. S8 (for separate inversions of isotropic structure and anisotropy) and Fig. 6 (for a joint inversion). Across the island, *Pn* velocities vary by $\pm$0.30 km s^{-1} about a mean of 8.10 km s^{-1}, with regions of higher- and lower-than-average velocities spread across the island. The *Pn* anisotropy ranges between 0 per cent to a maximum of 9.1 per cent and exhibits a very complex pattern. Both isotropic (by running an inversion with no anisotropy included) and anisotropic inversions yield similar patterns of higher and lower velocities across the island (Fig. S8a versus Fig. 6, respectively), with only slight differences in velocity amplitudes (except for a low-velocity zone along the northern part of the East coast, $\sim$16°S–18°S, which is near the edge of the resolved region). We also ran an inversion that solves only for the anisotropy (i.e. allowing no velocity variations, Fig. S8b). The result shows a very similar pattern and magnitude of anisotropy as in Fig. 6. Consequently, it appears that the anisotropy does not have a strong effect on isotropic lateral variations in *Pn* velocity and vice versa. The patterns of both velocity and anisotropy variations are stable.

The static delay variation of stations spanned 1.1 s, from -0.6 to $+0.5$ s, with a rms station delay of 0.2 s (Fig. S9). The static delay is a result of seismic heterogeneities near the station, the average crustal velocity, and the Moho depth. Positive station delays are representative of slower and/or thicker crust, while negative delays represent thinner and/or faster crust (such as for the two Mozambique channel stations). The variation of station static delays of 1.1 s is on par with the variation of the Moho location beneath Madagascar (Andriampenomanana *et al.* 2017); a variation of 1 s in the station delay corresponds to either a change of $\sim$10.4 km in crustal thickness or a variation of $\sim$1.6 km s^{-1} in crustal velocity (if the crustal thickness is fixed to 40 km, Hearn & Ni 1994).

6.1 *Pn* velocity variations

The average *Pn* velocity of 8.10 km s^{-1} is similar to the average *Pn* velocity of 8.10–8.20 km s^{-1} found beneath many other continental shields (e.g. Bamford 1977; Mooney & Braile 1989; Christensen & Mooney 1995). *Pn* velocities of 8.10–8.40 km s^{-1} have also been reported for unrifted Precambrian terranes in East Africa (e.g. Braile *et al.* 1994; Brazier *et al.* 2000; Langston *et al.* 2002). In many parts of the island, the *Pn* velocities are 8.20–8.30 km s^{-1}, typical of stable cratonic lithosphere, with no evidence of large scale pervasive structures that could signal recent or ongoing tectonic activity.

However, within the overall background of *Pn* velocities typical of stable continental regions, there are several areas with lower *Pn* velocities. The two areas with the lowest *Pn* velocities, between 7.85 and 8.00 km s^{-1}, corresponding to a $\sim$2–3 per cent velocity decrease, are found in the northern and central parts of Madagascar and correlate spatially with the NMAP and CMAP (Figs 1 and 6). Velocity errors in these areas are much smaller than the amplitude of the velocity anomalies (NMAP: 0.12 km s^{-1} compared to 0.25 km s^{-1}; and CMAP: 0.06 km s^{-1} compared to 0.20 km s^{-1}). There are other regions with *Pn* velocities of 7.97–8.05 km s^{-1}, just moderately lower than the 8.10 km s^{-1} average: one area is just north of the CMAP, one is to the south of the CMAP, and one is in the SMAP region (Figs S8a and 6). In addition, there are weak low velocity anomalies along the eastern coast near latitudes 18°S and 22°S, and an even weaker one at 24°S. A reduction in *Pn* velocity of $<$0.1 km s^{-1} may not be resolvable by our model, and in addition the strength of the northeastern coast anomaly seems to suffer from some cross-talk with anisotropic structure (Fig. S8a versus Fig. 6).

Laboratory measurements indicate that variations in the seismic velocities of *in situ* upper mantle rocks (e.g. peridotite) are linked to temperature, pressure and compositional variations, as well as changes in other physical properties (e.g. grain size, crystal orientation, presence of fluids) (e.g. Sato *et al.* 1989; Goes *et al.* 2000; Mainprice *et al.* 2000). Given the spatial correlation

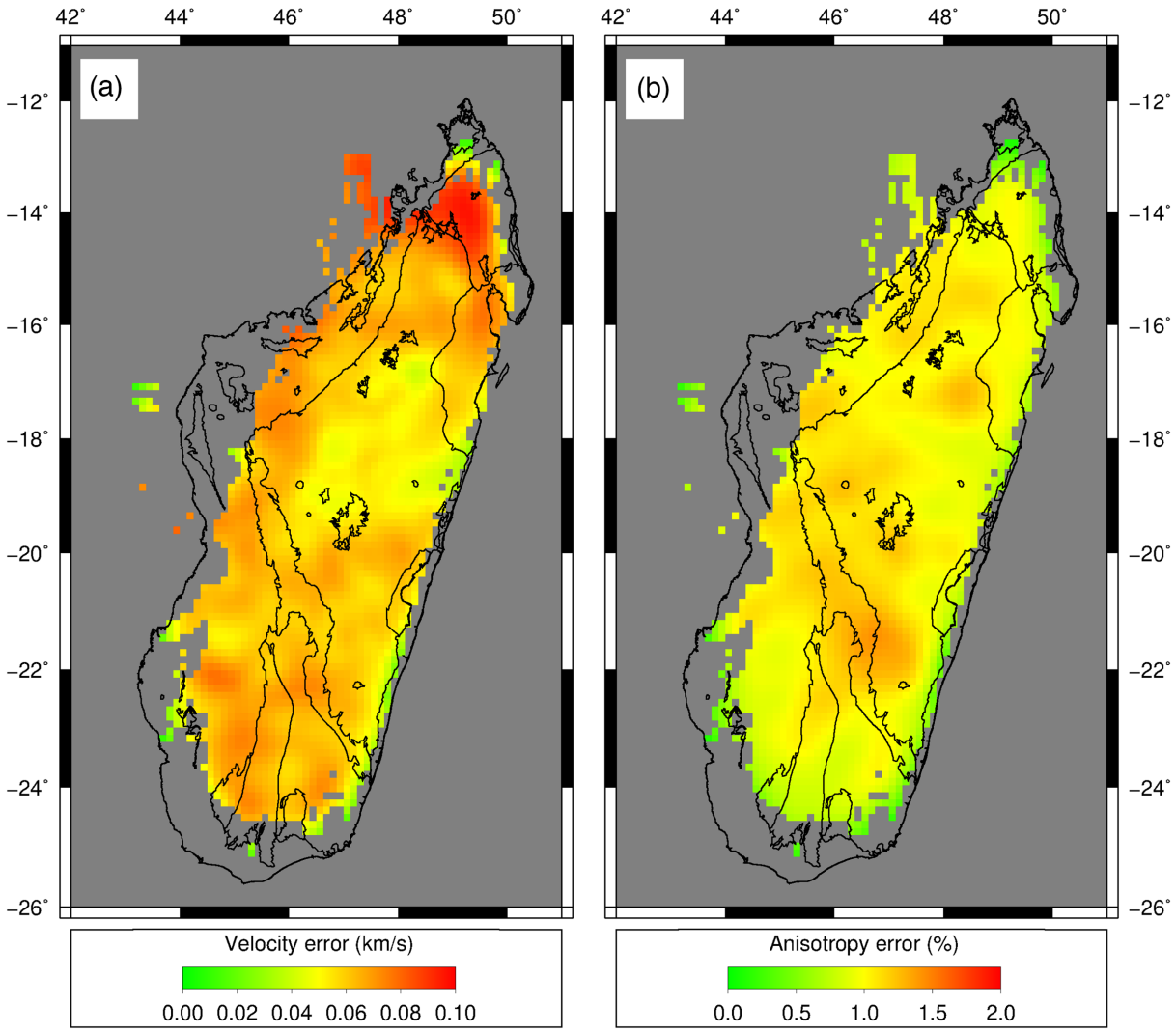

Figure 4. Standard errors of (a) the velocity and (b) anisotropy obtained from the bootstrap resampling technique using velocity and anisotropy damping coefficients of 500 and 600, respectively. Errors are generally less than 0.06 km s^{-1} for the velocity and less than 1 per cent for the anisotropy. The major geological unit boundaries shown in Fig. 1 are outlined.

between the regions of lower *Pn* velocities and the Cenozoic volcanic provinces in the Massif du Tsaratanàna (in the NMAP) and in the Itasy and Ankaratra region (in the CMAP), we attribute the reduction in *Pn* velocities in these regions to changes in uppermost mantle temperatures. Goes *et al.* (2000) show that an increase in temperature of 100 K results in a 0.5–2 per cent reduction in compressional wave speed. Thus, using the Goes *et al.* (2000) *Vp*-temperature scaling, the ∼2 per cent reduction in *Pn* under the CMAP and NMAP regions indicates an increase in uppermost mantle temperatures of 100–300 K. Temperatures at the high end (+300 K) could result in partial melting, consistent with the results of Melluso *et al.* (2018) which show, using isotopic and geochemical analyses of basanites from the CMAP, that there could be a small amount of partial melting beneath the region. A reduction of *Pn* velocities of about 2 per cent beneath the NMAP indicates that uppermost mantle temperatures beneath the northern part of the island may have also been perturbed by a few hundred degrees.

A thermal bulge beneath the CMAP was first proposed by Bertil & Regnoult (1998) to explain the diffuse seismic activity in this region, mostly accommodated within the lower crust. Subsequent seismological studies have also argued for thermally perturbed mantle lithosphere in central Madagascar to explain the horst-graben structures (Rindraharisaona *et al.* 2013) and high elevations (Andriampenomanana *et al.* 2017) within the central plateau. Pratt *et al.* (2017) used surface wave tomography to image regions of low *S*-wave velocities in the upper mantle beneath all of the Cenozoic volcanic provinces (NMAP, CMAP and SMAP). They argued that the low-velocity regions correspond to thermal anomalies produced by upwelling asthenospheric mantle-derived materials; and that for the CMAP, removal of the mantle lithosphere may be the cause of the upwelling. Our *Pn* velocity model is in good agreement with the surface wave tomography model of Pratt *et al.* (2017, Fig. 7). To first order, regions of lower *Pn* velocity (Fig. 7a) correlate spatially with regions of lower *S* velocity (Fig. 7b), even though more restricted in extent. Taking into consideration the spatial resolution in *Pn* velocity, which is as small as 1 × 1, the good correlation between the *Pn* wave model, which samples just a few kilometres beneath the Moho, and the surface wave model, which integrates the structure over much larger depth extent, indicates that the large-scale thermal

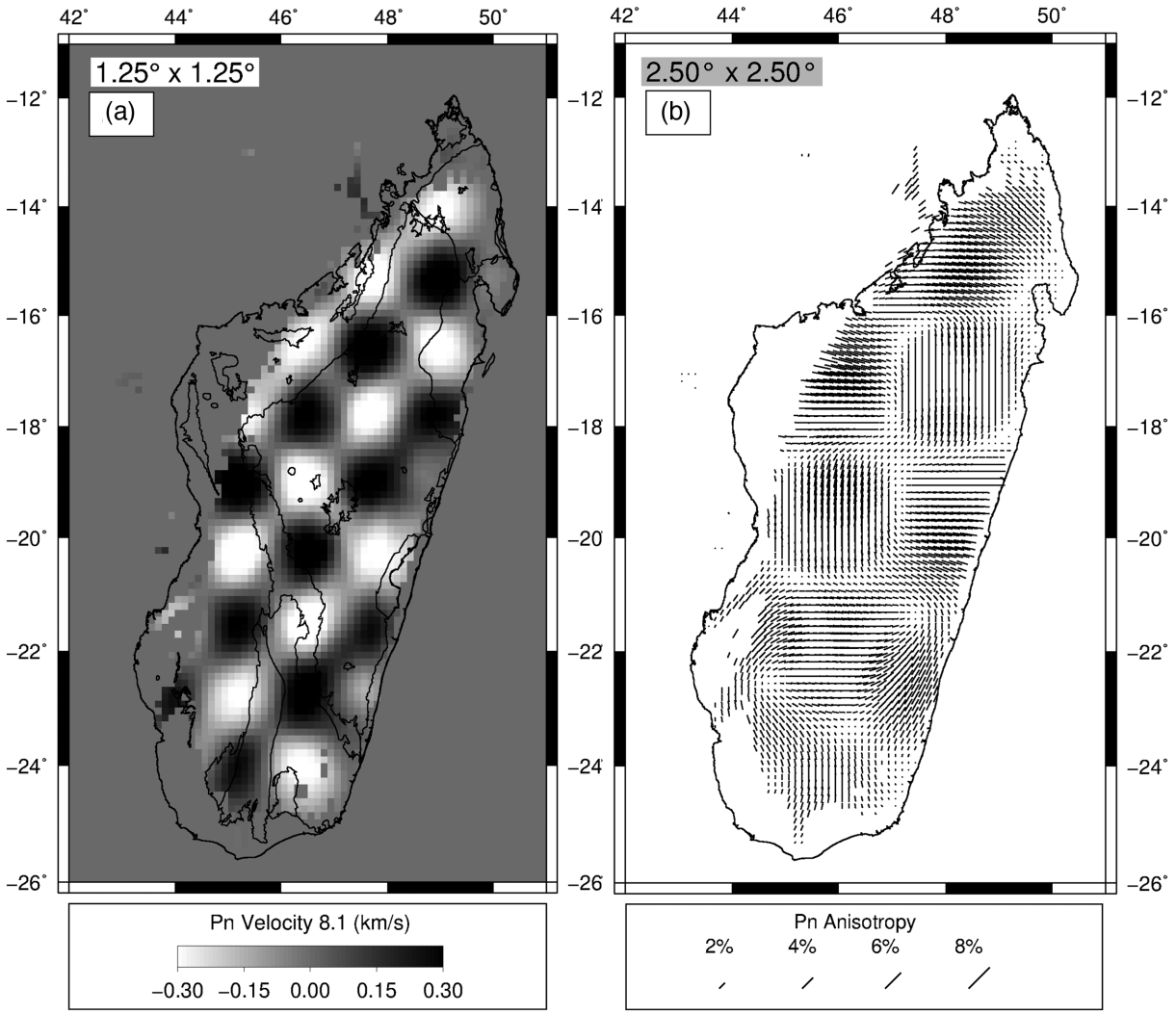

Figure 5. Checkerboard test results for (a) velocity and (b) anisotropy. The checkerboard size, which indicates the smallest resolution that can be resolved by the tomographic inversion, is 1.25° × 1.25° for velocity and 2.50° × 2.50° for anisotropy. The input checkerboard model consisted of velocity varying sinusoidally between −0.3 and +0.3 km s^{-1} relative to the average *Pn* velocity (8.1 km s^{-1}), and the anisotropy directions were set to alternate between N–S and E–W directions with sinusoidal variations in anisotropy strength of 9 per cent. The major geological unit boundaries shown in Fig. 1 are outlined.

anomaly within the asthenosphere, which has eroded some of the continental lithosphere, extends from the asthenosphere to at least the base of the crust.

Another interesting observation from the current study is the broad correlation of seismically active regions and low-*Pn*-velocity zones. Fig. 7a plots the seismicity in Madagascar from the Rakotondraibe *et al.* (2020) study, on top of our *Pn* velocity model. Seismotectonic studies in Madagascar revealed that earthquakes, especially in the central region, can occur in the lower crust (Bertil & Regnoult 1998; Rindraharisaona *et al.* 2013; Rakotondraibe *et al.* 2020). The correlation between lower-crustal earthquakes and the low-*Pn*-velocity areas might be related to magmatic activity. Focal mechanism studies in central Madagascar show predominantly normal faulting (Rindraharisaona *et al.* 2013; Rakotondraibe *et al.* 2020), consistent with crustal dyking.

6.2 *Pn* anisotropy variations

Pn azimuthal anisotropy beneath Madagascar shows complex local variations (Fig. 6). Unlike the *Pn* velocity variations, the *Pn* anisotropy pattern is highly variable, which is typical of many *Pn* studies (e.g. Mutlu & Karabulut 2011; Zhou & Lei 2016). In addition, the range of anisotropy (0–0.30 km s^{-1}, equivalent to 0–9.1 per cent) is comparable to other *Pn*-tomography studies conducted in other geographic regions (e.g. Bamford 1977; Christensen 1984; Hearn 1996). Previous studies show that *Pn* anisotropy directions may be influenced by absolute plate motion, shear strain from tectonic forces, subduction-driven deformation, fracture zones, fluid-filled cracks, partial melt or small-scale convective flow within the uppermost mantle (e.g. Bamford 1977; Hearn 1996; Smith & Ekström 1999).

In general, changes in the direction of anisotropy do not coincide with major geologic features in the region (Fig. 6). We compare our *Pn* anisotropy results with other anisotropy measurements that have been recently conducted in Madagascar to better understand the source of anisotropy. Fig. 6 and Supplementary Fig. S8(b) show estimates of seismic anisotropy from recent shear wave (*SKS*) splitting measurements (Reiss *et al.* 2016; Ramirez *et al.* 2018; Scholz *et al.* 2018) along with our *Pn* tomography and azimuthal anisotropy results. While the horizontally propagating *Pn* waves

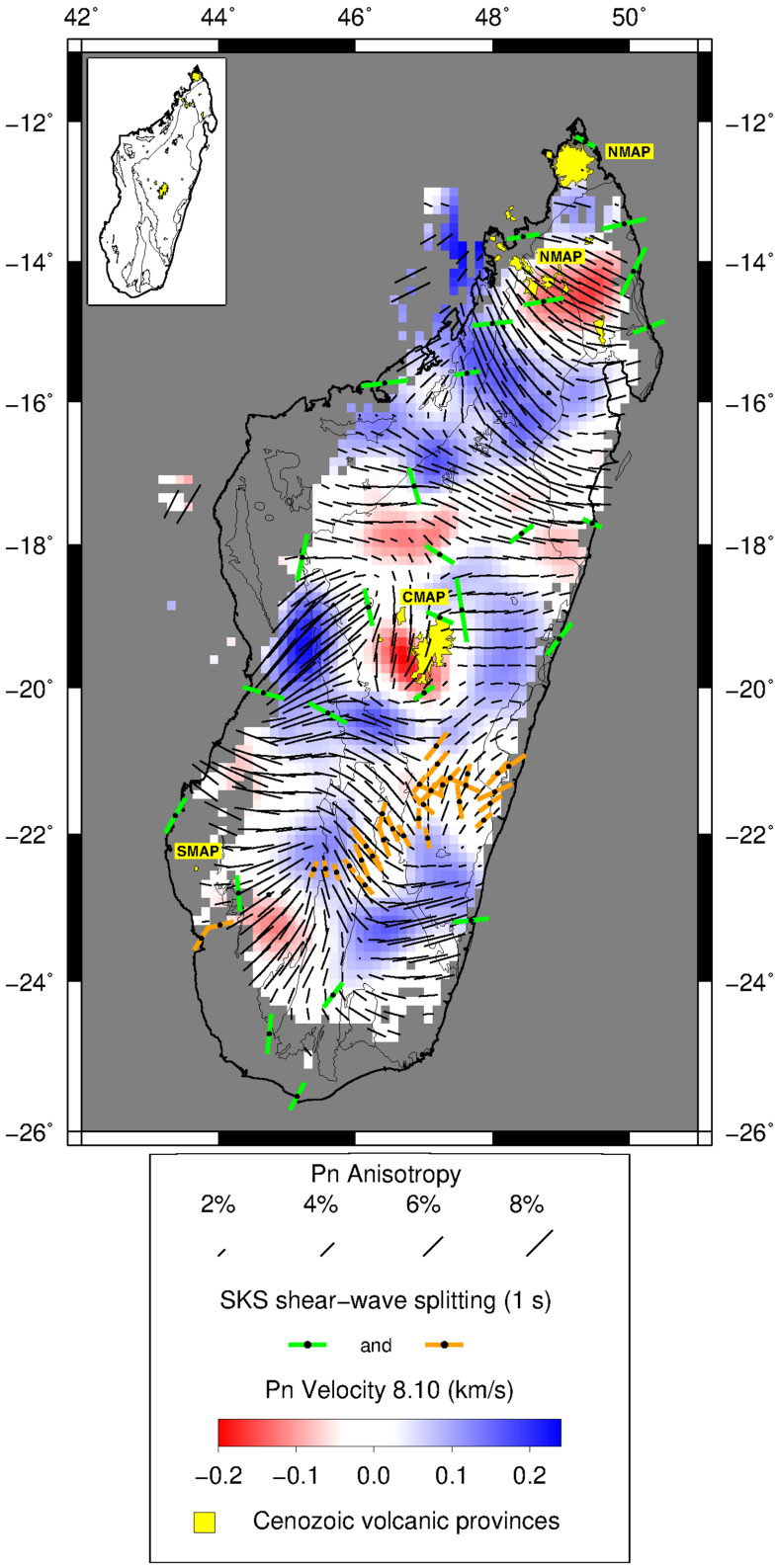

Figure 6. Map showing the lateral variation of *Pn* velocity (colour scale) and anisotropy (black bars) determined in this study, together with *SKS* shear wave splitting measurements from Reiss *et al.* (2016) (orange bars) and Ramirez *et al.* (2018) (green bars). Red and blue colours correspond to low and high *Pn*-velocity, respectively. Black bars indicate the fast *Pn*-anisotropy direction. The length of the bars is proportional to the anisotropy magnitude. Upper left-hand inset: map showing the major geological unit boundaries in Fig. 1.

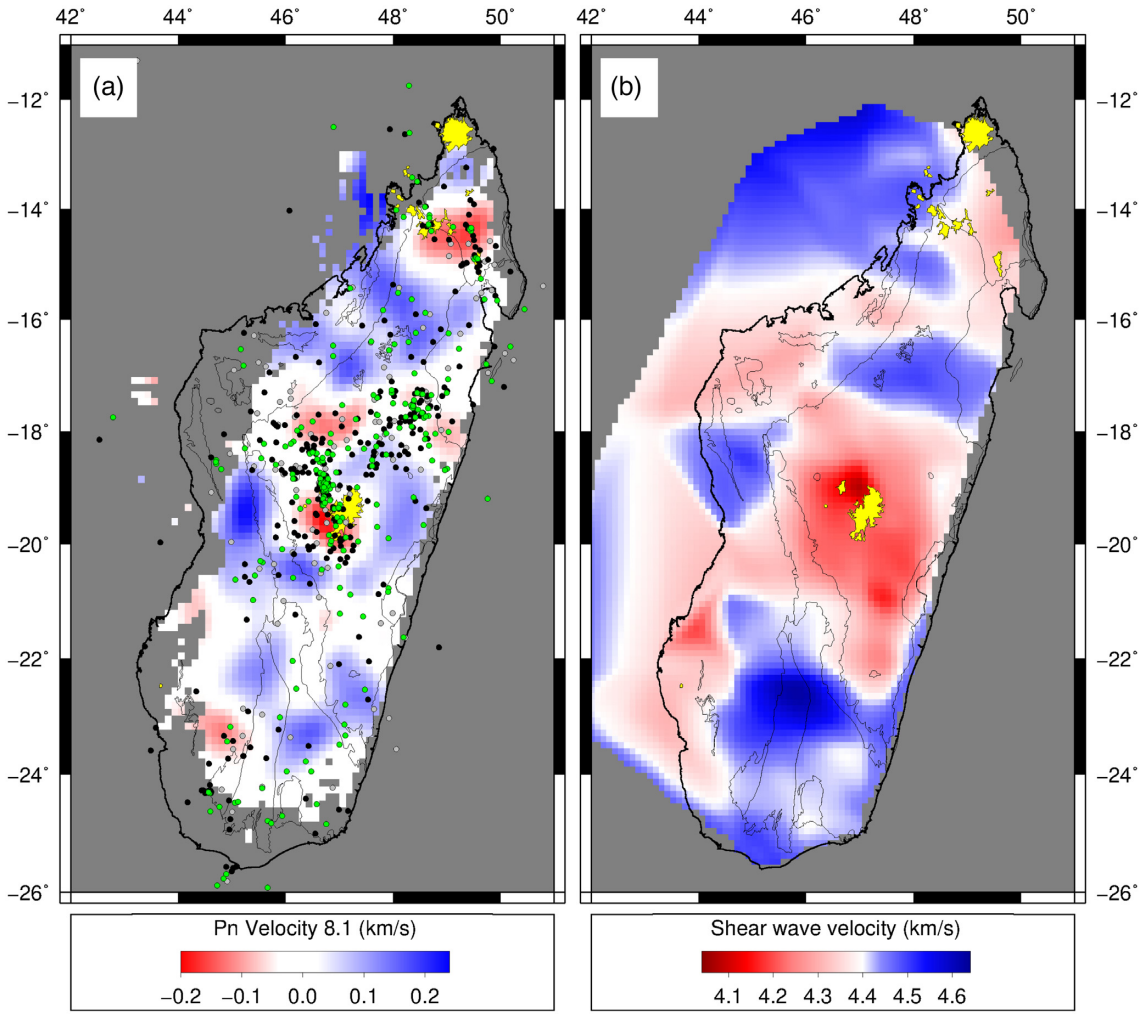

Figure 7. Map showing the lateral variations of (a) *Pn* velocity in the uppermost mantle, from this study, and (b) shear wave velocity at a depth of 50 km, from Pratt *et al.* (2017). Also plotted in (a) are earthquake epicentres from Rakotondraibe *et al.* (2020): green dots are events with depth <20 km, black dots are for depths ≥20 km, and grey dots are events located with high depth uncertainty (SEZ > 5.35 km). There is a good correlation between event locations and low-*Pn*-velocity zones. The major geological unit boundaries shown in Fig. 1 are outlined.

provide a depth-sensitive measure of anisotropy, restricted to the uppermost mantle (few kilometres beneath the Moho), *SKS* waves integrate anisotropy along their vertical paths through the upper mantle (e.g. Silver & Chan 1991). Therefore, a comparison between *Pn* and *SKS* anisotropy measurements can potentially provide insights about the depth of anisotropic layers and radial distribution of mantle deformation. In particular, *Pn* and *SKS* measurements that show similar anisotropic patterns suggest coherent deformation between the lithospheric and sublithospheric upper mantle, and that fossil anisotropy in the mantle lithosphere could be the primary source of anisotropy.

We will focus on regions with good resolution of anisotropy, taking into consideration the anisotropy error. In northern Madagascar, the *Pn* anisotropy direction is oriented NW–SE, while the *SKS* fast-polarization direction is significantly different, trending ENE–WSW. Ramirez *et al.* (2018) attributed the *SKS* fast-polarization directions in this region to a sublithospheric source: a NE-oriented mantle flow, associated with plate motion or the African superplume, modified by SE-oriented mantle flow from the Comores hotspot. The discrepancy between *Pn* and *SKS* anisotropy directions indicates that seismic anisotropy in northern Madagascar cannot be explained with a single anisotropic layer and that *Pn* anisotropy directions here are not linked to recent tectonic activity but could instead reveal frozen lithospheric mantle structures. As an exception to this general pattern, there is a strong correlation between *Pn* and *SKS* anisotropy direction in southcentral Madagascar, which will be discussed in Section 6.3.

Given the complicated collisional history of the Precambrian terranes that make up most of Madagascar, as well as the fact that uppermost mantle velocities do not show evidence of thermal modification of the uppermost mantle, except beneath the Cenozoic volcanic provinces, we attribute the complicated *Pn* anisotropy patterns to the complexity of fossil anisotropy in the upper part of the lithospheric mantle resulting from Precambrian tectonic events. It is difficult to determine whether the rifting of Madagascar from Africa overprinted the fossil anisotropy from Precambrian tectonothermal events because our results only cover the easternmost parts of the Mesozoic rifts along the western side of Madagascar. *Pn* anisotropy and velocity have resolutions restricted to the uppermost mantle, and so cannot constrain deeper lithospheric mantle structures that could signify much of the rifted passive margin.

6.3 Anisotropy beneath continental scale shear zones and crust–mantle coupling

An open question in plate tectonics is the depth extent of deformation visible at Earth's surface, particularly the deformation associated with large shear zones that accommodate important horizontal relative motions between crustal blocks, such as the San Andreas and the North Anatolian fault systems. Are these boundaries restricted to the crust, or do they root deeper in the upper mantle? Are they manifest as a single anisotropic layer or two independent layers of deformation? Southern Madagascar is a suitable region to explore these questions in a 'frozen' system (i.e. fossil anisotropy), since this area is characterized by several large-scale shear zones formed during the Pan-African orogenic events. In particular, shearing in southern Madagascar has resulted from the indentation of the rigid Neoarchean Antananarivo into the Mesoproterozoic Ikalamavony domain during the Pan-African orogeny (Schreurs *et al.* 2010).

A clear parallel between the outcropping crustal fabric, *Pn* fast directions, and the *SKS* fast directions (NW and NE directions, Figs 1 and 8) is observed in southcentral Madagascar, around the Ranotsara shear zone. Reiss *et al.* (2016) and Scholz *et al.* (2018) attributed the *SKS* fast polarization directions to fossil anisotropy in the lithosphere. The agreement between *Pn* and *SKS* anisotropy patterns supports such an interpretation, and suggests pervasive homogeneous deformation over the whole lithospheric mantle. Our new observations, along with previous studies of crustal radial anisotropy (Dreiling *et al.* 2018) and *SKS* anisotropy (Reiss *et al.* 2016; Ramirez *et al.* 2018; Scholz *et al.* 2018), suggest that the whole crust and lithospheric mantle have preserved this broad deformation for hundreds of millions of years since the Pan-African orogenies and that both were deformed coherently. This idea is supported by the orientation of the large-scale outcropping tectonic structures (e.g. Martelat *et al.* 2000) that are parallel to the *Pn* anisotropy observed in horizontally propagating waves sampling the uppermost mantle and parallel to the fast split *SKS* waves, vertically integrating the underlying lithosphere deformation. This coherency of deformation over the whole lithosphere implies a strong crust–mantle coupling at the time that the deformation occurred and a rooting of the shear zone within the upper mantle (Vauchez *et al*. 2012), as proposed by Bonnin *et al.* (2010) for the San Andreas fault system. Such a hypothesis suggests that anisotropy in the mantle lithosphere (seen by *Pn* and *SKS*) has the same age as the deformation observed in the outcropping rocks, that is dating from the late Pan-African tectonic episode (Martelat *et al.* 2000). In such areas of homogeneous deformation through the whole lithosphere, one can therefore expect a crustal contribution of a few tenths of seconds to the overall *SKS* splitting measurements (Barruol & Mainprice 1993), and the observed delay times reflect the integrated effect of the anisotropy of the whole lithosphere.

However, in most other parts of the island there is little agreement between the *SKS* fast-polarization directions reported by Ramirez *et al.* (2018) and the orientation of *Pn* anisotropy. The apparent crust-mantle coupling observed in southern Madagascar is clearly not visible beneath the other shear zones affecting the central and northern parts of the island. For instance, in central Madagascar, the NS-trending Angavo shear zone (Raharimahefa *et al.* 2013) is underlain by low *Pn* anisotropy trending roughly EW. Interestingly, this area corresponds to a high V_{Pn} area and low *Vs* area (Figs 6 and 7), suggesting that a possible asthenospheric upwelling and/or lithospheric delamination has removed or erased the uppermost mantle Pan-African fabric. Ramirez *et al.* (2018) invoked a combination of fossil anisotropy in the mantle lithosphere and flow in the asthenosphere to explain the complicated pattern of fast polarization directions. The discrepancy between *Pn* and *SKS* anisotropy directions in many parts of the island indicates that the *SKS* anisotropy cannot be attributed to a single layer and likely results from the integration of vertically varying anisotropy. In these regions, strain within the lithosphere has different origins at different depths. Seismology cannot constrain the age of each tectonic episode nor the precise depth of the boundary between the deformed layer within the uppermost mantle (sampled by *Pn*) and the rest of the lithosphere (integrated by *SKS* phases).

Madagascar is clearly a promising place for investigating this first order question of the tectonic coupling between the crust and mantle and the vertical partitioning of strain within Earth. Future dedicated experiments should focus on the frozen outcropping shear zones to better characterize the vertical distribution of anisotropy within the crust and the upper mantle.

6.4 A plate boundary crossing Madagascar?

A number of studies have proposed that a diffuse plate boundary separating the Lwandle Plate from the Somalian Plate could cross the central part of Madagascar (e.g. Horner-Johnson *et al.* 2007; Saria *et al.* 2013; Stamps *et al.* 2014). Alternatively, there are recently several lines of evidence that counter its existence. Focal mechanisms reported in a recent seismotectonic study of Madagascar show mostly normal faulting with strike directions mostly oriented perpendicular to the axis of the proposed plate boundary, indicating E–W extension (Rakotondraibe *et al.* 2020).

The northern edge of the Lwandle Plate could coincide with the region of slightly lower *Pn* velocities ($\sim$0.13 km s^{-1}) just to the north of the CMAP (Figs 1 and 6). However, the *Pn* anisotropy pattern is highly variable in this region, with orientations ranging from W–E to NW–SE, which is not consistent with a uniform sense of deformation expected for a plate boundary. The same is true for most of the *SKS* splitting measurements in the area, which tend to be at a high angle to the proposed boundary (Ramirez *et al.* 2018).

A second geometry of diffuse plate boundary is implicitly proposed by Michon (2016). It corresponds to a NS-trending zone crossing the whole Madagascar Island and accommodating a weak E–W extension that could represent the southern termination of the Somalia-Nubia relative motion and, therefore, a branch of the East-African Rift system. The Comores archipelago could represent such a zone of lithospheric transfer between the East-African Rift and Madagascar. This model would expect a rather simple anisotropic pattern of EW-trending fast directions, which is clearly not observed. This absence of direct correlation of anisotropy (*Pn* and *SKS*) with a simple plate boundary may result from the very weak deformations involved that could be accommodated without erasing the complex anisotropy patchwork inherited from past tectonic events and still dominate the anisotropy signatures at the various depths of investigation.

The present study, therefore, does not show evidence of the existence of a plate boundary developing across this region. However, diffuse deformation observed at crustal levels could signify incipient and diffuse extension due to the southern termination of the East-African Rift.

7 SUMMARY AND CONCLUSIONS

We have imaged the lateral variation of *Pn* velocity and anisotropy within the uppermost mantle of Madagascar by inverting the traveltime residuals of *Pn* phases. A least-square fit of the relationship

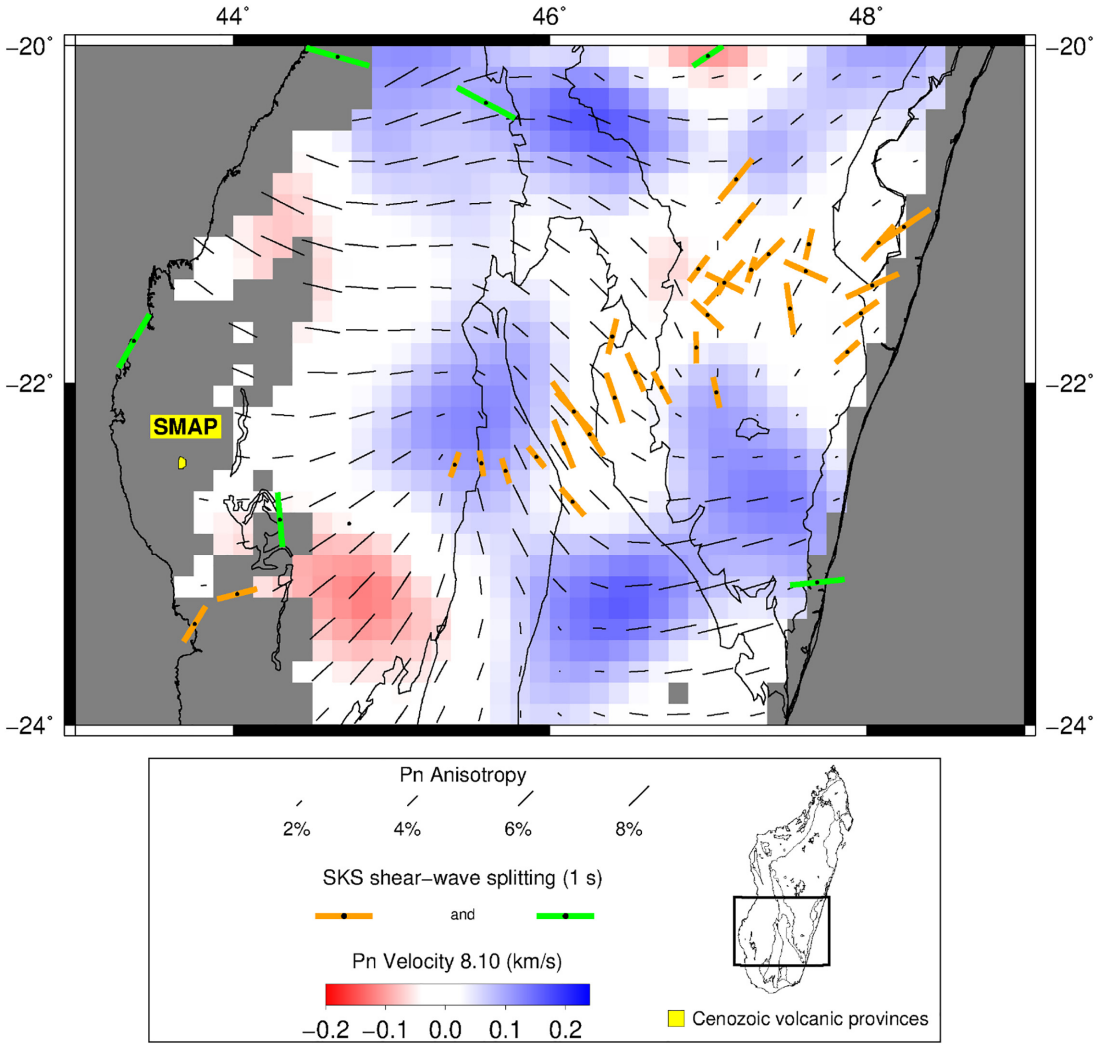

Figure 8. Lateral variation of *Pn* velocity, *Pn* anisotropy, and *SKS* shear wave splitting in southcentral Madagascar. As discussed in the text, the consistent alignment of crustal tectonic lineaments, *Pn* fast azimuths, and *SKS* fast split directions indicate a coherent pattern of deformation through the entire lithosphere and therefore suggest crust-mantle coupling at the time that the shear zones in southern Madagascar developed. The major geological unit boundaries shown in Fig. 1 are outlined.

between traveltime and distance of the *Pn* phases indicates that the average *Pn* velocity of the uppermost mantle beneath Madagascar is approximately 8.10 km s^{-1} and ranges from 7.80 to 8.40 km s^{-1}. A maximum value of ±0.30 km s^{-1} is observed, equivalent to 9.1 per cent in *Pn* anisotropy.

Low-*Pn*-velocity (<8.00 km s^{-1}) zones are observed directly beneath the alkaline volcanic provinces in the northern and central region of Madagascar, indicating that uppermost mantle temperatures may be elevated by a few hundred degrees. These low velocity zones are presumably linked to the Cenozoic intraplate volcanism of Madagascar. However, compared to the model of Pratt *et al.* (2017), the low-*Pn*-velocity zones are more restricted in lateral extent. High-*Pn*-velocity zones (>8.20 km s^{-1}) coincide with stable regions and are less seismically active compared to low-*Pn*-velocity zones. *Pn* anisotropy patterns in Madagascar are very complex, reflecting a complicated mantle fabric originating from Precambrian tectonothermal events. A good match between *Pn* anisotropy and *SKS* splitting is only observed in southern Madagascar and associated with the large-scale Pan-African strike-slip shear zone, suggesting a crust–mantle coupling when those structures were active. Our results provide little support for the existence of an incipient (Lwandle) plate boundary developing across central Madagascar.

ACKNOWLEDGEMENTS

We gratefully acknowledge the field support from IRIS-PASSCAL, which provided the seismic equipment for the MACOMO project; and IRIS, GEOFON and GEOSCOPE for additional seismic data. This research was funded by the National Science Foundation, through grant EAR-0838426. RHUM-RUM seismological deployments were supported by the French ANR (fra) (Agence Nationale de la Recherche, project ANR-11-BS56-0013) and by the DFG (Deutsche Forschungsgemeinschaft) grant SI1538/2-1 RHUM-RUM in Germany, by the French CNRS-INSU (Institut National des Sciences de l'Univers, Centre National de la Recherche Scientifique (fra)), program SYSTER, by the CNRS-INEE (Institut Ecologie et Environnement) and the TAAF (Terres Australes et Antarctiques Françaises). RHUM-RUM equipment was provided by the Alfred Wegener Institut (AWI) in Bremerhaven, Germany, and

by RESIF-SISMOB in Grenoble, France. The equipment for SELASOMA by the GIPP (Geophysical Instrument Pool Potsdam), GeoForschungsZentrum in Potsdam and the fieldwork was supported by the DFG. The support of the National Research Foundation through the DST/NRF South African Research Chairs Initiative (SARChI) is also acknowledged. We also thank an anonymous reviewer and Stewart Fishwick for providing insightful reviews which helped to improve the paper. Figures in this paper have been produced with GMT (Wessel & Smith 1998). The datasets analyzed in the current study are freely available online, please visit the digital object identifiers (DOIs) cited in the data section.

REFERENCES

Andriampenomanana, F. *et al.*, 2017. The structure of the crust and uppermost mantle beneath Madagascar, *Geophys. J. Int.,* **210,** 1525–1544.

Bamford, D., 1977. *Pn* velocity anisotropy in a continental upper mantle, *Geophys. J. R. astr. Soc.,* **49,** 29–48.

Bardintzeff, J-M., Liegeois, J-P., Bonin, B., Bellon, H. & Rasamimanana, G., 2010. Madagascar volcanic provinces linked to the Gondwana breakup: Geochemical and isotopic evidences for contrasting mantle sources, *Gondwana Res.,* **18,** 295–314.

Barruol, G. & Mainprice, D., 1993. A quantitative evaluation of the contribution of crustal rocks to the shear wave splitting of teleseismic SKS waves, *Phys. Earth planet. Inter.,* **78**(3–4), 281–300.

Barruol, G. & Sigloch, K., 2013. Investigating La Réunion hot spot from crust to core, *EOS, trans. Am. geophys. Un.,* **94,** 205–207.

Bertil, D. & Regnoult, J. M., 1998. Seismotectonics of Madagascar, *Tectonophysics,* **294,** 57–74.

Besairie, H., 1971. *Tectonique de Madagascar*. Tectonique de l' Afrique, Sciences de la Terre UNESCO Paris, pp. 549–558.

Bonnin, M., Barruol, G. & Bokelmann, G.H.R., 2010. Upper mantle deformation beneath the north American-Pacific plate boundary in California from SKS splitting, *J. geophys. Res.,* **115**(B4), doi:10.1029/2009JB006438.

Braile, L.W., Wang, B., Daudt, C.R., Keller, G.R. & Patel, J.P., 1994. Modeling the 2-D seismic velocity structure across the Kenya rift, *Tectonophysics,* **236,** 251–269.

Brazier, R., Nyblade, A.A., Langston, C.A. & Owens, T.J., 2000. Pn wave velocities beneath the Tanzania Craton and adjacent rifted mobile belts, East Africa, *Geophys. Res. Lett.,* **27,** 2365–2368.

Buchwaldt, R., Tucker, R.D. & Dymek, R.F., 2005. Geochemistry and geochronology of a Miocene volcanic suite from Mt. Tsaratanana, northern Madagascar. Goldschmidt 2005 Conference Abstracts A241.

Cesca, S. *et al.*, 2020. Drainage of a deep magma reservoir near Mayotte inferred from seismicity and deformation, *Nat. Geosci.,* **13,** 87–93.

Christensen, N.I., 1984. The magnitude, symmetry and origin of upper mantle anisotropy based on fabric analyses of ultramafic tectonites, *Geophys. J. R. astr. Soc.,* **76,** 89–111.

Christensen, N. I. & Mooney, W.D., 1995. Seismic velocity structure and composition of the continental crust: a global view, *J. geophys. Res.,* **100,** 9761–9788.

Collins, A.S., 2006. Madagascar and the amagalmation of the central Gondwana, *Gondwana Res.,* **9,** 3–6.

Dreiling, J., Tilmann, F., Yuan, X., Giese, J., Rindraharisaona, E.J., Rümpker, G. & Wysession, M.E., 2018. Crustal radial anisotropy and linkage to geodynamic processes: a study based on seismic ambient noise in southern Madagascar, *J. geophys. Res.,* **123,** 5130–5146.

Emerick, C.M. & Duncan, R.A., 1982. Age progressive volcanism in the Comores Archipelago, western Indian Ocean and implications for Somali plate tectonics, *Earth planet. Sci. Lett.,* **60,** 415–428.

GEOFON Data Centre, 1993. *GEOFON Seismic Network*. Deutsches GeoForschungsZentrum GFZ. doi:10.14470/TR560404.

Goes, S., Govers, R. & Vacher, P., 2000. Shallow mantle temperatures under Europe from P and S wave tomography, *J. geophys. Res.,* **105,** 11 153–11 169.

Hearn, T.M., 1996. Anisotropic *Pn* tomography in the western United States, *J. geophys. Res,* **101,** 8403–8414.

Hearn, T.M. & Ni, J.F., 1994. *Pn* velocities beneath continental collision zones: the Turkish-Iranian Plateau, *Geophys. J. Int.,* **117,** 273–283.

Horner-Johnson, B.C., Gordon, R.G. & Argus, D.F., 2007. Plate kinematic evidence for the existence of a distinct plate between the Nubian and Somalian plates along the Southwest Indian Ridge, *J. geophys. Res.,* **112,** B05418.

Institut De Physique Du Globe De Paris (IPGP) & Ecole Et Observatoire Des Sciences De La Terre De Strasbourg (EOST), 1982. *GEOSCOPE, French Global Network of broad band seismic stations*. Institut de Physique du Globe de Paris (IPGP). doi:10.18715/GEOSCOPE.G.

Koch, M., 1992. Bootstrap inversion for vertical and lateral variations of the S wave structure and the vp/vs-ratio from shallow earthquakes in the Rhine graben seismic zone, Germany, *Tectonophysics,* **210,** 91–115.

Lahr, J.C., 1999, revised 2012, HYPOELLIPSE: a computer program for determining local earthquake hypocentral parameters, magnitude, and first-motion pattern: U.S. Geological Survey Open-File Report 99-23, version 1.1, 119 p. and software, available at http://pubs.usgs.gov/of/1999/ofr-99-0023/.

Langston, C.A., Nyblade, A.A. & Owens, T.J., 2002. Regional wave propagation in Tanzania, East Africa, *J. geophys. Res.,* **107**(B1), ESE1–1-ESE 1-18.

Mainprice, D., Barruol, G. & Ben Ismail, W., 2000. The seismic anisotropy of the Earth's mantle: from single crystal to polycrystal, in *Earth's Deep Interior: Mineral Physics and Tomography from the Atomic to the Global Scale,* eds, Karato, S.I. *et al.*, pp. 237–264, AGU.

Martelat, J.-E., Lardeaux, J.-M., Nicollet, C. & Rakotondrazafy, R., 2000. Strain pattern and Late Precambrian deformation history in southern Madagascar, *Precambrian Res.,* **102,** 1–20.

Martelat, J.-E., Randrianasolo, B., Schulmann, K., Lardeaux, J.-M. & Devidal, J.-L., 2014. Airborne magnetic data compared to petrology of crustal scale shear zones from southern Madagascar: A tool for deciphering magma and fluid transfer in orogenic crust, *J. Afr. Earth Sci.,* **94,** 74–85.

Melluso, L., Tucker, R.D., Cucciniello, C., le Roex, A.P., Morra, V., Zanetti, A. & Rakotoson, R.L, 2018. The magmatic evolution and genesis of the Quaternary basanite-trachyphonolite suite of Itasy (Madagascar) as inferred by geochemistry, Sr-Nd-Pb isotopes and trace element distribution in coexisting phases, *Lithos,* **310–311,** 50–64.

Michon, L., 2016. The volcanism of the Comores archipelago integrated at a regional scale, in *Active Volcanoes of the Southwest Indian Ocean: Piton de la Fournaise and Karthala. Active Volcanoes of the World,* pp. 333–344. eds, Bachelery, P., Lenat, J.-F., Di Muro, A. & Michon, L., Springer-Verlag.

Mooney, W.D. & Braile, L.W., 1989. The seismic structure of the continental crust and upper mantle of North America, in *The Geology of North America-An Overview,* Vol. **A,** pp. 39–52. eds, Bally, A.W. & Palmer, A.R., Geol. SOC. Am.

Mutlu, A.K. & Karabulut, H., 2011. Anisotropic Pn tomography of Turkey and adjacent regions, *Geophys. J. Int.,* **187,** 1743–1758.

Nougier, J., Cantagrel, J.M. & Karche, J.P., 1986. The Comores archipelago in the western Indian Ocean: volcanology, geochronology and geodynamic setting, *J. Afr. Earth Sci.,* **5,** 135–144.

Pei, S., Sun, Y. & Nafi Toksöz, M., 2011. Tomographic Pn and Sn velocity beneath the continental collision zone from Alps to Himalaya, *J. geophys. Res.,* **116,** B10311.

Pratt, M.J. *et al.*, 2017. Shear-velocity structure of the crust and upper mantle of Madagascar derived from surface wave tomography, *Earth planet. Sci. Lett.,* **458,** 405–417.

Rabinowitz, P.D., Coffin, M.F. & Falvey, D., 1983. The separation of Madagascar and Africa, *Science,* **220,** 67–69.

Raharimahefa, T., Kusky, T.M., Toraman, E., Rasoazanamparany, C. & Rasaonina, I., 2013. Geometry and kinematics of the late Proterozoic Angavo Shear Zone, Central Madagascar: implications for Gondwana Assembly, *Tectonophysics,* **592,** 113–129.

Rajaonarison, T.A., Stamps, D.S., Fishwick, S., Brune, S., Glerum, A. & Hu, J., 2020. Numerical modeling of mantle flow beneath Madagascar to

constrain upper mantle rheology beneath continental regions, *J. Geophys. Res. Solid Earth,* **125,** e2019JB018560.
Rakotondraibe, T. *et al.*, 2020. Seismicity and seismotectonics of Madagascar revealed by the 2011–2013 deployment of the island-wide MACOMO broadband seismic array, *Tectonophysics,* **790,** 228547, doi:10.1016/j.tecto.2020.228547.
Ramirez, C., Nyblade, A.A., Wysession, M.E., Pratt, M.J, Andriampenomanana, F. & Rakotondraibe, T., 2018. Complex seismic anisotropy in Madagascar revealed by shear wave splitting measurements, *Geophys. J. Int.,* **215,** 1718–1727.
Reiss, M. C., Rümpker, G., Tilmann, F., Yuan, X., Giese, J. & Rindraharisaona, E.J., 2016. Seismic anisotropy of the lithosphere and asthenosphere beneath southern Madagascar from teleseismic shear wave splitting analysis and waveform modeling, *J. geophys. Res.,* **121,** 6627–6643.
Rindraharisaona, E.J., Guidarelli, M., Aoudia, A. & Rambolamanana, G., 2013. Earth structure and instrumental seismicity of Madagascar: implications on the seismotectonics, *Tectonophysics,* **594,** 165–181.
Rindraharisaona, E.J., Tilmann, F., Yuan, X., Rümpker, G., Giese, J., Rambolamanana, G. & Barruol, G., 2017. Crustal structure of southern Madagascar from receiver functions and ambient noise correlation: Implications for crustal evolution, *J. Geophys. Res. Solid Earth,* **122,** 1179–1197.
Saria, E., Calais, E., Altmamini, Z., Pascal, P. & Farah, H., 2013. A new velocity field for Africa from combined GPS and Doris: contribution to African reference frame, *J. geophys. Res.,* **118,** 1677–1697.
Saria, E., Calais, E., Stamps, D.S., Delvaux, D. & Hartnady, C.J.H., 2014. Present-day kinematics of the East African Rift, *J. geophys. Res.,* **119,** 3584–3600.
Sato, H., Sacks, I.S. & Murase, T., 1989. The use of laboratory velocity data for estimating temperature and partial melt fraction in the low-velocity zone: comparison with heat flow and electrical conductivity studies, *J. geophys. Res.,* **94,** 5689–5704.
Schreurs, G., Giese, J., Berger, A. & Gnos, E., 2010. A new perspective on the significance of the Ranotsara shear zone in Madagascar, *Int. J. Earth Sci.,* **99,** 1827–1847.
Scholz, J.-R., Barruol, G., Fontaine, F.R., Mazzullo, A., Montagner, J.P., Stutzman, E., Michon, L. & Sigloch, K., 2018. SKS splitting in the Western Indian Ocean from land and seafloor seismometers: plume, plate and ridge signatures, *Earth planet. Sci. Lett.,* **498,** 169–184.
Scripps Institution of Oceanography, 1986. IRIS/IDA Seismic Network. International Federation of Digital Seismograph Networks. Dataset/Seismic Network. 10.7914/SN/II. doi:10.7914/SN/II.
Shackleton, R.M., 1996. The final collision zone between East and West Gondwana: where is it?, *J. Afr. Earth Sci.,* **23,** 271–287.
Silver, P. & Chan, W., 1991. Shear wave splitting and subcontinental mantle deformation, *J. geophys. Res.,* **96,** 16 429–16 454.
Smith, D.P. & Ekström, G., 1999. A global Pn anisotropy beneath continents, *J. geophys. Res.,* **104,** 963–980.
Stamps, D.S., Flesch, L.M., Calais, E. & Ghosh, A., 2014. Current kinematics and dynamics of Africa and the East African Rift System, *J. geophys. Res.,* **119,** 5161–5186.
Stamps, D.S., Iaffaldano, G. & Calais, E., 2015. Role of mantle flow in Nubia-Somalia divergence, *Geophys. Res. Lett.,* **42,** 290–296.
Stamps, D.S., Saria, E. & Kreemer, C., 2018. A geodetic strain rate model for the East African Rift system, *Sci. Rep.,* **8,** doi:10.1038/s41598-017-19097-w.
Tilmann, F., Yuan, X., Rümpker, G. & Rindraharisaona, E., 2012. SELASOMA Project, Madagascar 2012–2014, DeutschesGeoForschungsZentrum GFZ, Seismic Network. doi:10.14470/MR7567431421.
Tucker, R.D., Peters, S.G., Roig, J.Y., Théveniaut, H. & Delor, C., 2012. *Notice explicative des cartes géologique et métallogéniques de la République de Madagascar à 1/1000000,* Ministère des Mines, PGRM, Antananarivo, République de Madagascar.
Tucker, R.D., Roig, J.-Y., Delor, C., Amelin, Y., Goncalves, P., Rabarimanana, M.H., Ralison, A.V. & Belcher, R.W., 2011. Neoproterozoic extension in the Greater Dharwar Craton: a reevaluation of the "Betsimisaraka suture" in Madagascar, *Can. J. Earth Sci.,* **48,** 389–417.
Vauchez, A., Tommasi, A. & Mainprice, D., 2012. Faults (shear zones) in the Earth's mantle. *Tectonophysics,* **558–559**(C), 1–27.
Wessel, P. & Smith, W.H., 1998. New, improved version of Generic Mapping Tools released, *EOS, Trans. Am. Geophys. Un.,* **79,** 579–579.
Wysession, M., Wiens, D. & Nyblade, A., 2011. Investigation of Sources of Intraplate Volcanism Using PASSCAL Broadband Instruments in Madagascar, the Comores, and Mozambique, International Federation of Digital Seismograph Networks. Other/Seismic Network. doi:10.7914/SN/XV_2011.
Zhou, Z. & Lei, J., 2016. Pn anisotropic tomography and mantle dynamics beneath China, *Phys. Earth planet. Inter.,* **257,** 193–204.

SUPPORTING INFORMATION

Supplementary data are available at *GJI* online.

Figure S1. Examples of (a) clear pick arrival (event on 25 January 2013–23:37:00 in Table S2), (b) a noisier but accepted arrival (event on 12 August 2012–17:55:16 in Table S2) and (c) a noisy data that was rejected. These waveforms are from different stations.
Figure S2. *Pn*-velocity models produced using a range of velocity damping coefficients (50–2000) with the anisotropy component turned off.
Figure S3. Trade-off between the velocity-damping coefficients and data fit coefficients. The three pairs of maps show the *Pn* velocity (left-hand panel) and error (right-hand panel) from the inversions calculated using three different damping values (A = 50, B = 500, C = 2000). Note that over-damping (C) gives poor resolution but a lower error, while under-damping (A) provides a higher resolution, but unrealistic features with a larger error. The best damping value, which gives the acceptable model, is obtained at the 'knee' of the curve (B = 500). Therefore, a damping coefficient of 500 is used for further analysis.
Figure S4. Plot of the velocity-to-anisotropy and anisotropy-to-velocity trade-offs. The best value of the anisotropy damping constant would equalize the velocity-to-anisotropy and anisotropy-to-velocity trade-offs. The damping that corresponds to the intersection of both curves (grey star) is the best anisotropy damping coefficient for the inversion (∼600).
Figure S5. Fast *Pn*-anisotropy direction, inverted with no velocity variations, using three different damping values (A = 100, B = 600, C = 2000). A damping value of 600 (B) was used in the preferred model.
Figure S6. Recovered checkerboard *Pn* velocities from the tomographic inversions using different checkerboard sizes (1.00° × 1.00°, 1.25° × 1.25°, 1.50° × 1.50°, 1.75° × 1.75°, 2.0° × 2.0°, 2.25° × 2.25°, 2.50° × 2.50°, 2.75° × 2.75° and 3.00° × 3.00°). The input checkerboard model consisted of velocities varying sinusoidally between −0.30 and +0.30 km s^{-1} relative to the average *Pn* velocity (8.10 km s^{-1}), with the input anisotropy set to zero but anisotropy being inverted for in a joint inversion.
Figure S7. Recovered checkerboard *Pn* anisotropy values from the tomographic inversions using different checkerboard sizes (1.00° × 1.00°, 1.25° × 1.25°, 1.50° × 1.50°, 1.75° × 1.75°, 2.0° × 2.0°, 2.25° × 2.25°, 2.50° × 2.50°, 2.75° × 2.75° and 3.00° × 3.00°). The input checkerboard model consisted of anisotropy directions set to alternate between N–S and E–W directions with sinusoidal variations in anisotropy strength of 9 per cent. The isotropic velocity perturbations were set to zero in the input model, but were free to vary in the joint inversion.
Figure S8. *Pn*-velocity and anisotropy, plotted together with the major geological unit boundaries shown in Fig. 1. (a) Uppermost mantle isotropic *Pn*-velocity variations (inverted with no anisotropy included and a velocity damping coefficient of 500). Red and blue colours correspond to low and high *Pn*-velocity, respectively. (b)

Fast *Pn*-anisotropy direction (inverted with no velocity variations and an anisotropy damping coefficient of 600). Black bars indicate the fast *Pn*-anisotropy direction determined in this study. The length of the bars is proportional to the anisotropy magnitude. *SKS* shear wave splitting data from Reiss *et al.* (2016) (orange bars) and Ramirez *et al.* (2018) (green bars) is also shown. The strike and length of the bars indicate the fast-velocity direction of *SKS* shear wave splitting and the amount of splitting, respectively.

Figure S9. Static station delay times. Circles and squares denote negative and positive delays, respectively, with radii proportional to the size of the station delays. Positive station delays are representative of slower and/or thicker crust, while negative delays indicate thinner and/or faster crust.

Table S1. Permanent and temporary broad-band seismic stations used in this study.

Table S2. List of 343 local and regional seismic events used in the inversion.

Please note: Oxford University Press is not responsible for the content or functionality of any supporting materials supplied by the authors. Any queries (other than missing material) should be directed to the corresponding author for the paper.